

Dynamical Monte Carlo investigation of spin reversals and nonequilibrium magnetization of single-molecule magnets

Gui-Bin Liu and Bang-Gui Liu*

*Institute of Physics, Chinese Academy of Sciences, Beijing 100190, China
Beijing National Laboratory for Condensed Matter Physics, Beijing 100190, China*

(Dated: December 9, 2019)

In this paper, we combine thermal effects with Landau-Zener (LZ) quantum tunneling effects in a dynamical Monte Carlo (DMC) framework to produce satisfactory magnetization curves of single-molecule magnet (SMM) systems. We use the giant spin approximation for SMM spins and consider regular lattices of SMMs with magnetic dipolar interactions (MDI). We calculate spin reversal probabilities from thermal-activated barrier hurdling, direct LZ tunneling, and thermal-assisted LZ tunnelings in the presence of sweeping magnetic fields. We do systematical DMC simulations for Mn_{12} -ac systems with various temperatures and sweeping field rates. Our simulations produce clear step structures in low-temperature magnetization curves, and our results show that the thermally activated barrier hurdling becomes dominating at high temperature near 3K and the thermal-assisted tunnelings play important roles at intermediate temperature. Our magnetization curves are satisfactory compared to experimental results, considering possible defects and misalignments in actual samples. Furthermore, our DMC results show that the MDI, with the thermal effects, have important effects on the LZ tunneling processes, but both the MDI and the LZ tunneling give place to the thermal-activated barrier hurdling effect in determining the magnetization curves when the temperature is near 3K. This DMC approach can be applicable to other SMM systems, and could be used to study other properties of SMM systems.

PACS numbers: 75.75.-c, 05.10.-a, 75.78.-n, 75.10.-b, 75.90.+w

I. INTRODUCTION

Single-molecule magnet (SMM) systems have been attracting more and more attention because they can be used to make devices for spintronic applications^{1,2}, quantum computing³, high-density magnetic information storage⁴, and so on⁵. Usually, a SMM can be treated as a large spin with strong magnetic anisotropy at low temperature. The most famous and typical is Mn_{12} -ac ($[Mn_{12}O_{12}(Ac)_{16}(H_2O)_4] \cdot 2HAc \cdot 4H_2O$, where HAc=acetic acid), or Mn_{12} for short⁶. It usually has spin $S = 10$ and large anisotropy energy, producing a high spin reversal barrier⁷. When put on appropriate substrates such as gold and silicon^{4,8}, SMMs can form two-dimensional ferromagnetic materials through substrate-induced constructive spin interactions^{9,10}. One of the most intriguing phenomena observed in SMM systems is low-temperature step-wise structure in magnetization curves¹¹⁻¹³. Great effort have been made to investigate this phenomenon and related effects¹⁴⁻²¹. The step-wise structure is attributed to Landau-Zener (LZ) quantum tunneling effect^{22,23}. This stimulates intensive study on LZ model and its variants²⁴⁻³². Some authors use numeric diagonalization methods^{33,34} to study many-level LZ models to understand experimental magnetization curves. However, it is difficult to consider thermal effects in these approaches to obtain satisfactory magnetization curves comparable to experimental results.

In this paper, we shall combine the thermal effects with the LZ quantum tunneling effects in a dynamical Monte Carlo (DMC) framework^{35,36} to produce satisfactory magnetization curves comparable to experimental

results. We consider ideal lattices consistent with experimental ones and assume that there are no defects and axis-misalignments therein. We use the giant spin approximation for spins of SMMs and consider only magnetic dipolar interactions for comparison with experimental results. We calculate spin reversal probabilities from thermal-activated barrier hurdling, direct LZ tunneling effect, and thermal-assisted LZ tunneling effects in the presence of sweeping magnetic fields. Taking the Mn_{12} as example, we do systematical DMC simulations with various temperatures and sweeping field rates. Our magnetization curves are satisfactory compared to experimental results. Interplays of the LZ tunneling effect, the thermal effects, and the magnetic dipolar interactions are elucidated. More detailed results will be presented in the following.

The rest of this paper is organized as follows. In next section we shall define our spin model and approximation strategy. In the third section we shall describe our simulation method, present the probability formula for the three spin reversal mechanisms, and give our simulation parameters. In the fourth section we shall present our simulated magnetization curves and some analysis. In the fifth section we shall show the key roles of the dipolar interactions. Finally, we shall give our conclusion in the sixth section.

II. SPIN MODEL AND APPROXIMATION

Without losing generality, we take typical Mn_{12} system as our sample in the following. Under giant spin approxi-

mation, every Mn_{12} SMM is represented by a spin $S=10$. Magnetic dipolar interactions are the only inter-SMM interactions, with hyperfine interactions neglected. Mn_{12} SMMs are arranged to form a body-centered tetragonal lattice with experimental lattice parameters³⁷. Using a body-centered tetragonal unit cell that consists of two SMMs, we define our lattice as $L_1 \times L_2 \times L_3$, where L_1 , L_2 , and L_3 are three positive integers. A longitudinal magnetic field $B_z(t) = B_0 + \nu t$ is applied along the c -easy axis of magnetization, where ν is the field-sweeping rate and B_0 is the starting magnetic field. The total Hamiltonian of this system can be expressed as

$$\hat{H} = \sum_i \hat{H}_i^0 + \frac{1}{2} \sum_{i \neq j} \hat{H}_{ij}^{\text{di}}, \quad (1)$$

where \hat{H}_i^0 is the single-body part for the i -th single SMM, and \hat{H}_{ij}^{di} describes the magnetic dipolar interaction between the i -th and j -th SMM. The factor $1/2$ before the sum sign is due to the double counting in the summation. \hat{H}_i^0 is given by

$$\begin{aligned} \hat{H}_i^0 = & -D(\hat{S}_i^z)^2 + E[(\hat{S}_i^x)^2 - (\hat{S}_i^y)^2] \\ & + B_4^0 \hat{O}_4^0 + B_4^4 \hat{O}_4^4 + g\mu_B B_z \hat{S}_i^z, \end{aligned} \quad (2)$$

where $\hat{\mathbf{S}}_i \equiv (\hat{S}_i^x, \hat{S}_i^y, \hat{S}_i^z)$ is the spin vector operator for the i -th SMM, g the Landé g-factor (here $g = 2$ is used), μ_B the Bohr magneton, D , E , B_4^0 and B_4^4 are all anisotropic parameters, and \hat{O}_4^0 and \hat{O}_4^4 are both Steven operators¹⁹ defined by $\hat{O}_4^0 = 35(\hat{S}_i^z)^4 - [30S(S+1) - 25](\hat{S}_i^z)^2 + 3S^2(S+1)^2 - 6S(S+1)$ and $\hat{O}_4^4 = [(\hat{S}_i^+)^4 + (\hat{S}_i^-)^4]/2$. \hat{H}_{ij}^{di} is defined by

$$\hat{H}_{ij}^{\text{di}} = \frac{\mu_0 g^2 \mu_B^2}{4\pi r_{ij}^3} [\hat{\mathbf{S}}_i \cdot \hat{\mathbf{S}}_j - \frac{3}{r_{ij}^2} (\hat{\mathbf{S}}_i \cdot \mathbf{r}_{ij})(\hat{\mathbf{S}}_j \cdot \mathbf{r}_{ij})], \quad (3)$$

where μ_0 is the magnetic permeability of vacuum, and \mathbf{r}_{ij} the vector from i to j , with $r_{ij} = |\mathbf{r}_{ij}|$ being the distance between i and j .

For the i -th SMM, we treat all the effects from the other SMMs by classical-spin approximation. As a result, we derive the partial Hamiltonian \hat{H}_i that acts on the i -th SMM:

$$\begin{aligned} \hat{H}_i = & \hat{H}_i^0 + g\mu_B \mathbf{B}_i^{\text{di}} \cdot \hat{\mathbf{S}}_i \\ = & -D(\hat{S}_i^z)^2 + B_4^0 \hat{O}_4^0 + \hat{H}_i^{\text{tr}} + g\mu_B (B_z + B_{iz}^{\text{di}}) \hat{S}_i^z, \end{aligned} \quad (4)$$

where the transverse part \hat{H}_i^{tr} is defined as

$$\hat{H}_i^{\text{tr}} = E[(\hat{S}_i^x)^2 - (\hat{S}_i^y)^2] + B_4^4 \hat{O}_4^4 + g\mu_B (B_{ix}^{\text{di}} \hat{S}_i^x + B_{iy}^{\text{di}} \hat{S}_i^y). \quad (5)$$

For the i -th SMM, the dipolar interaction of the other SMMs is equivalent to $\mathbf{B}_i^{\text{di}} \equiv (B_{ix}^{\text{di}}, B_{iy}^{\text{di}}, B_{iz}^{\text{di}}) = \sum_{j(\neq i)} \mathbf{B}_{ji}$, where \mathbf{B}_{ji} is the magnetic dipolar field applied by the j -th SMM on the i -th SMM. It contributes a magnetic field consisting of longitudinal and transverse parts.

III. SIMULATION METHOD AND PARAMETERS

There are three main mechanisms related to spin reversal^{7,11-14,19,24,27}: (a) thermal-activated barrier hurdling, (b) direct LZ tunneling, and (c) thermal-assisted LZ tunneling. They are shown in Fig. 1. The thermal-activated barrier hurdling dominates at high temperature and the direct LZ tunneling at low temperature [if the blocking temperature T_B ($\sim 3.3\text{K}$ for Mn_{12})¹⁷ is treated as high temperature], and the thermal-assisted LZ tunneling at intermediate temperature. For the time scale we are interested, we need not treat phonon-related interactions directly, but use an effective transition-state theory to calculate the thermal-activated probability and spin reversal rate in the following.

When calculating the thermal energy barrier we ignore the small transverse part \hat{H}_i^{tr} and use classical approximation for the spin operators. The large spin $S = 10$ of Mn_{12} further makes the approximations more accurate. As a result, the energy of the i -th SMM can be expressed as

$$E_i = -D_2(S_i^z)^2 - D_4(S_i^z)^4 + h_i S_i^z, \quad (6)$$

where S_i^z is the classical variable for the spin operator \hat{S}_i^z , $h_i = g\mu_B (B_z + B_{iz}^{\text{di}})$, $D_2 = D + [30S(S+1) - 25]B_4^0$, and $D_4 = -35B_4^0$.

We define our MC steps by the time points, $t_n = \Delta t \cdot n$, where n takes 0, 1, 2, 3, and so on. Because each of the spins has two equilibrium orientations ($S_i^{\text{eq}} = \pm S$) along the easy axis, we assume every spin takes either S or $-S$ at each of the times t_n . We use an angle variable θ_i to describe the i -th spin's deviation from its original orientation (set as $\theta_i = 0$). Naturally, $\theta_i = \pi$ is the reversed state. Then all the other angle values ($0 < \theta_i < \pi$) are the transition states. Expressing S_i^z as $S_i^{\text{eq}} \cos \theta_i$, we usually have a maximum in the curve of $E_i(\cos \theta_i)$, and the maximum determines the energy barrier for the spin reversal³⁸⁻⁴⁰, as shown in Fig. 1(a). We define $x_i = \cos \theta_i$ for convenience, and then have $-1 \leq x_i \leq 1$ for real θ_i . Under conditions $D_2 > 0$ and $D_4 > 0$, the barrier can be expressed as: $\Delta E_i^n = E_i(x_i^m)$ if $|x_i^m| \leq 1$; $\Delta E_i^n = E_i(-1) = |2h_i S_i^{\text{eq}}|$ if $x_i^m < -1$; $\Delta E_i^n = E_i(1) = 0$ if $x_i^m > 1$. Here, formally, x_i^m is defined as $\sqrt[3]{-q/2 + \sqrt{\Delta_d}} + \sqrt[3]{-q/2 - \sqrt{\Delta_d}}$, where $\Delta_d = (q/2)^2 + (p/3)^3$, $p = D_2/(2D_4 S^2)$, and $q = -h_i S_i^{\text{eq}}/(4D_4 S^4)$. These parameters are dependent on the spin configuration and thus on the time t_n (or n). Then the probability P_i^n for a thermal-activated spin reversal within the n -th MC step is defined by⁴¹

$$P_i^n = 1 - \exp(-\Delta t \cdot R_i^n), \quad (7)$$

where $R_i^n = R_0 \exp(-\frac{\Delta E_i^n}{k_B T})$, independent of time t within the region $[t_n, t_{n+1} = t_n + \Delta t]$, is the transition rate determined by Arrhenius law⁴², k_B is the Boltzmann constant and R_0 the characteristic attempt frequency. For

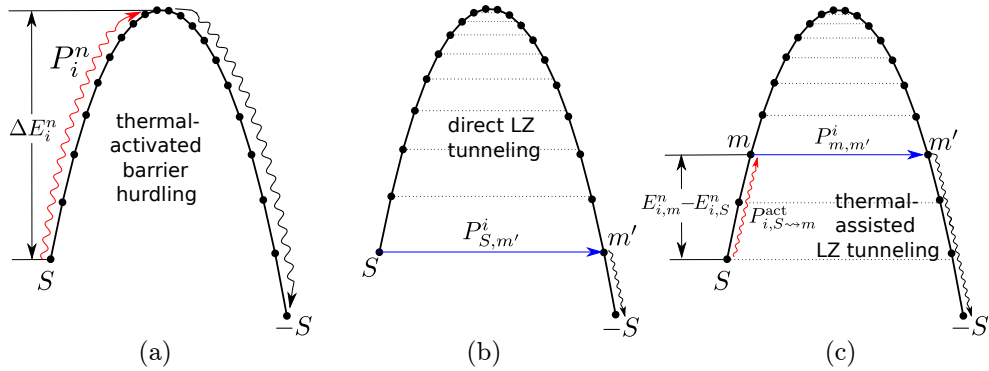


FIG. 1: (Color online.) A schematic demonstration for the three spin reversal mechanisms: (a) thermal-activated barrier hurdling, (b) direct LZ tunneling, and (c) thermal-assisted LZ tunneling. The horizontal solid line with arrow in (b) and (c) shows a pair of energy levels match for the resonance tunneling conditions. The horizontal dotted lines in (b) and (c), as guide for eyes, show that these pairs of energy levels do not match.

$\Delta t \ll 1/R_i^n$, Eq. (7) reduces to $P_i^n = \Delta t \cdot R_i^n$. The probability expression defined in Eq. (7) ensures that P_i^n will not exceed unity when Δt is very large with respect to $1/R_i^n$.

When temperature is lower than T_B , LZ tunneling begins to contribute to spin reversal. Hamiltonian Eq. (4) has $2S + 1$ energy levels, which to a first-order approximation can be labelled by $m = S, S-1, \dots, -(S-1), -S$ and denoted as $E_{i,m}^n$. Due to the existence of the transverse part \hat{H}_i^{tr} , these energy levels have avoided crossings when $B_z + B_{iz}^{\text{di}}$ equals $B_{m,m'}^i$, with m and m' taking values among $S, S-1, \dots, -(S-1), -S$. When B_z is swept to $B_{m,m'}^i - B_{iz}^{\text{di}}$ at which the avoided level crossing happens between two states m and m' , quantum tunneling occurs between the two states, and the tunneling can be well described using LZ tunneling^{10,18,33,34}. The nonadiabatic LZ tunneling probability $P_{m,m'}^i$ is given by^{22,23}

$$P_{m,m'}^i = 1 - \exp \left[-\frac{\pi(\Delta_{m,m'}^i)^2}{2\hbar g\mu_B|m - m'|\nu} \right], \quad (8)$$

where the tunnel splitting $\Delta_{m,m'}^i$ is the energy gap at the avoided crossing of states m and m' . $B_{m,m'}^i$ and $\Delta_{m,m'}^i$ can be calculated by diagonalizing Eq. (4). If the dipolar field is neglected, $B_{m,m'}^i$, $\Delta_{m,m'}^i$, and $P_{m,m'}^i$ reduce to $B_{m,m'}^0$, $\Delta_{m,m'}^0$, and $P_{m,m'}^0$, those of corresponding isolated SMMs, respectively.

At the beginning of field sweeping, we have the spin $m = S$. If $T \ll T_B$, thermal activations are frozen, and LZ tunnelings only occur at the avoided crossings (S, m') , where m' takes one of $-S, -S+1, \dots, S-1$. This is the direct tunneling and the tunneling probability is $P_{S,m'}^i$, determined by Eq. (8) [see Fig. 1(b)]. When the temperature is in the intermediate region $0 \ll T < T_B$, the thermal-assisted tunneling play an important role. This process can be represented by $S \rightsquigarrow m \rightarrow m' \rightsquigarrow -S$ as shown in Fig. 1(c), in which S and m states lie on one side of the thermal barrier and m' and $-S$ states on

the other side. The first process $S \rightsquigarrow m$ means that a spin is thermally activated from S to m state with the probability $P_{i,S \rightsquigarrow m}^{\text{act}}$ defined by Eq. (7), with $E_{i,m}^n - E_{i,S}^n$ substituted for ΔE_i^n . The second process $m \rightarrow m'$ is just the LZ tunneling at (m, m') , with the probability defined in Eq. (8). The third process $m' \rightsquigarrow -S$ represents that the spin relaxes quickly from the m' state to the $-S$ state^{13,43,44}. Therefore, the reversal probability of thermal-assisted tunneling at (m, m') is given by $P_{i,m \rightarrow m'}^{\text{assist}} = P_{i,S \rightsquigarrow m}^{\text{act}} P_{m,m'}^i$. We assume that a spin will have long enough time to transit to the possible lowest level at current field after the LZ tunneling is finished^{13,43,44}. Thus a spin will be reversed finally.

For the i -th SMM, we have $B_{m,-m}^i = 0$ for m taking every integer between S and $-S$, and all the other $B_{m,m'}^i$ ($m \neq -m'$) values differ from each other¹⁶. That is to say, when the field B_z is swept to $B_{m,m'}^i - B_{iz}^{\text{di}}$, if $B_{m,m'}^i \neq 0$, then either a direct tunneling ($m = S$) or a thermal-assisted tunneling ($m \neq S$) occurs. If we denote the reversal probability as P_i^{tunnel} in a unified form, then the total spin reversal probability from both thermal-activated barrier hurdling and the quantum tunneling ($m \neq -m'$) is given by

$$P_i^{n,\text{tot}} = 1 - (1 - P_i^n)(1 - P_i^{\text{tunnel}}). \quad (9)$$

This reduces to the sum $P_i^n + P_i^{\text{tunnel}}$ when both of the partial probabilities are small enough¹⁰. In the case of $B_{m,m'}^i = 0$, several thermal-assisted tunnelings can occur at the same field, and the total reversal probability is

$$P_i^{n,\text{tot}} = 1 - (1 - P_i^n)(1 - P_{S,-S}^i) \prod_{0 < m < S} (1 - P_{i,m \rightarrow -m}^{\text{assist}}). \quad (10)$$

Here, Eqs. (9) and (10) are both based on the assumption that different spin reversal mechanisms work independently. Actually, the processes that a reversed spin is reversed again are also considered, but the probabilities are tiny.

We use experimental lattice constants, $a = b = 17.1668 \text{ \AA}$ and $c = 12.1545 \text{ \AA}$, and experimental anisotropy parameters, $D/k_B = 0.66 \text{ K}$, $B_4^0/k_B = -3.2 \times 10^{-5} \text{ K}$, and $B_4^4/k_B = 6 \times 10^{-5} \text{ K}^{16,20,37}$. As for the second-order transverse parameter E , $E/k_B = 1.8 \times 10^{-3} \text{ K}$ is taken from the average of experimental values²¹. We take $\Delta t = 0.1 \text{ ms}$ and $R_0 = 10^9/\text{s}$, which guarantee the good balance between computational demand and precision. The dipolar fields (B_{ix}^{di} , B_{iy}^{di} , B_{iz}^{di}) at each SMM are updated whenever any of the SMM spins is reversed. The $\Delta_{m,m'}^i$ values are recalculated whenever any LZ tunneling happens. In the simulations, the field B_z is swept from -7 to 7 T in the forward process, and the full magnetization hysteresis loop is obtained simply by using the loop symmetry. Every magnetization curve is calculated by averaging over 100 runs to reduce statistical errors.

IV. SIMULATED MAGNETIZATION CURVES

Presented in Fig. 2 are simulated magnetization curves (with M normalized to the saturated value M_S) against the applied sweeping field B_z for ten different temperatures: 0.1, 0.5, 0.6, 0.8, 1.0, 1.5, 2.0, 2.5, 2.8, and 3.2 K. Here, the lattice dimension is $10 \times 10 \times 10$ and the field sweeping rate is 0.02 T/s . Each of the curves is calculated by averaging over 100 runs. The curves of 0.1 K and 0.5 K fall in the same curve, which implies that thermal activation is totally frozen under 0.5 K. It can be seen in Fig. 2 that the area enclosed by the magnetization loop decreases with the temperature increasing, becoming nearly zero at 3.2 K, near the blocking temperature 3.3 K of Mn_{12} . There are clear magnetization steps (having nearly vertical risers and horizontal treads) caused by LZ quantum tunneling when the temperature is 1.5 K and lower. The riser of each step is not completely vertical because of the dipolar interaction. At higher temperatures ($\geq 2.0 \text{ K}$), there is no complete step and there are only some kinks that remind us of some LZ tunneling. This should be caused mainly by thermal effects.

Presented in Fig. 3 are the right parts of the magnetization curves against the applied sweeping field for three temperatures, 0.1, 1.5, and 2.5 K, and with three sweeping rates, 0.002, 0.02, and 0.2 T/s. It is clear that for $T=0.1 \text{ K}$, almost only direct LZ tunneling happens, and the magnetization step risers from $B_z=2$ to 6 T in Fig. 3 correspond to $B_{S,m'}^0$ with m' being from -6 to 2 in Table I. For $T=1.5 \text{ K}$, some steps are still clear, but the step risers deviate substantially from the corresponding $B_{S,m'}^0$ values and the step treads are not still horizontal, which show that thermal-assisted LZ tunnelings play an important role. When temperature rises to 2.5 K, there is no complete step and only some kinks can be seen in the lower part. This is because the effects of thermal activation becomes dominating over the tunneling effects. Different sweeping rates lead to substantial changes in

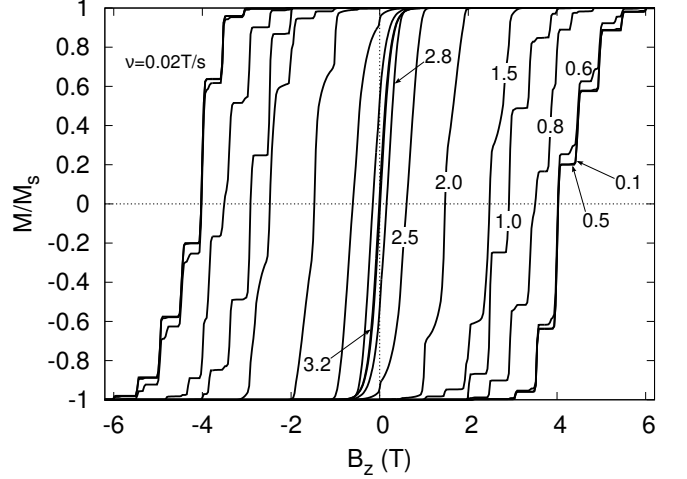


FIG. 2: Simulated magnetic hysteresis loops (M/M_S vs B_z) with sweeping rate $\nu = 0.02 \text{ T/s}$ for ten temperatures: 0.1, 0.5, 0.6, 0.8, 1.0, 1.5, 2.0, 2.5, 2.8, and 3.2 K (from outside to inside). The lattice dimension is $10 \times 10 \times 10$. Note that the two curves of 0.1 K and 0.5 K fall in the same curve.

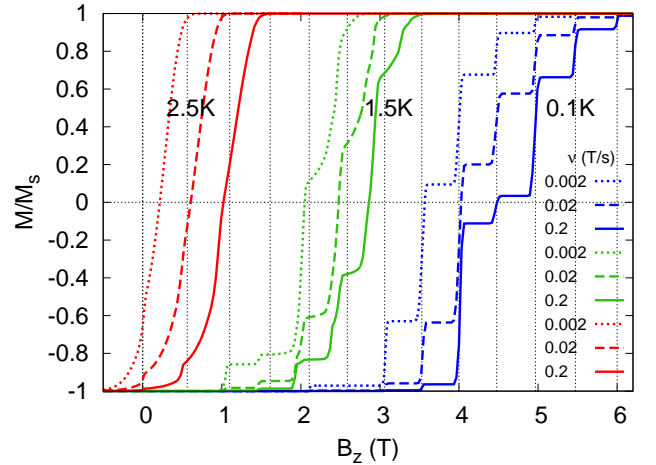


FIG. 3: (Color online.) The right parts of simulated magnetization curves of different field sweeping rates 0.002 (dot), 0.02 (dash), and 0.2 (solid) T/s for three temperatures 0.1 K, 1.5 K, and 2.5 K, as labelled. The lattice dimension is $10 \times 10 \times 10$. Each of the nearly vertical step risers, if can be seen, implies one of the magnetic fields at which the direct and thermal assisted LZ tunnelings take place. The thin vertical dotted lines show the B_z positions of $B_{S,m'}^0$ for $m' = -10, -9, \dots, 2$.

the hysteresis loops and the loop area increases with the sweeping rate.

Presented in Fig. 4 are the right parts of simulated hysteresis loops with $\nu=0.02 \text{ T/s}$ at three temperatures for three different lattice shapes: $10 \times 10 \times 10$ (box), $20 \times 20 \times 3$ (slab), and $3 \times 3 \times 100$ (rod). The temperatures are 0.1, 1.5, and 2.5 K. For comparison, the simulated results without the dipolar interaction are presented too. For $T=0.1 \text{ K}$, there are clear step structures for all the

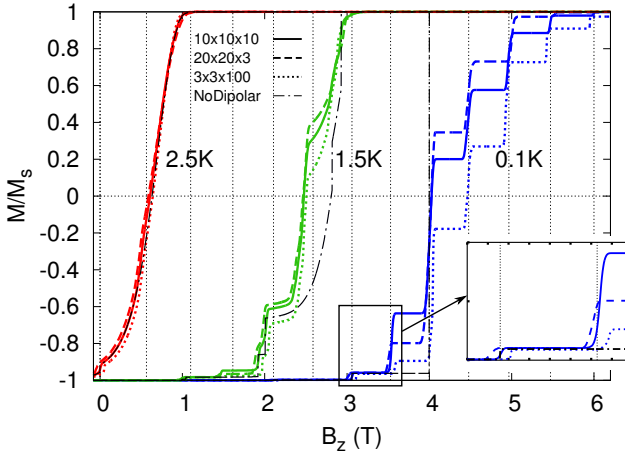


FIG. 4: (Color online.) The right parts of simulated magnetization curves with field sweeping rate 0.02 T/s for three different lattice dimensions: $10 \times 10 \times 10$ (solid), $20 \times 20 \times 3$ (dash), and $3 \times 3 \times 100$ (dot). For comparison, we also present the results without considering dipolar interaction (dash-dot). The inset is an amplified view of the small part. Temperatures are 0.1 K , 1.5 K , and 2.5 K , as labelled.

three lattice shapes. The step riser height varies with the lattice shape, which can be attributed to the dipolar interaction. When the dipolar interaction is switched off, there are only one tall step with the riser at $B_z = 4.00\text{ T}$ and one very short step with the riser at 3.06 T . When the temperature changes to 1.5 K , the hysteresis loops become substantially smaller. The step structures in the lower parts shown in Fig. 4 are deformed and those in the upper parts disappear. For $T=2.5\text{ K}$, there does not exist any step structure at all for all the four cases, and the lattice shape differences have only a little effect on the hysteresis loops. It can be seen clearly that the lattice shape plays important roles in determining the hysteresis loops and the dipolar interaction is necessary to make the simulated results consistent with experimental magnetization curves, especially at low temperatures.

The above simulated results show that the area enclosed by a magnetization hysteresis loop decreases with the temperature increasing and increases with the sweeping rate increasing. This is completely consistent with the temperature and sweeping-rate dependence of the thermal reversal probability and LZ tunneling probabilities. Thermal activation effects dominate at high temperature. The LZ tunneling effects manifest themselves through the steps and kinks along the magnetization curves. However, there is a limit for the hysteresis loops at the low temperature end for a given sweeping rate. These limiting magnetization curves are caused by the minimal reversal probability set by the direct LZ quantum tunneling effect because thermal activation probability becomes tiny at low temperatures. These results are consistent with experimental magnetization curves of good Mn_{12} crystals^{16,17}. The consistence should be sat-

isfactory, because our theoretical probabilities are calculated under leading order approximation and there are various defects and easy-axis misalignments in actual materials.

TABLE I: Calculated results of $B_{S,m'}^0$, $\Delta B_{S,m'}$, $P_{S,m'}^0$, $\langle P_{S,m'} \rangle$, and $\sigma_{S,m'}^P$ for the direct LZ tunneling (S, m') when the field B_z is swept to 3.75 T . $T = 0.5\text{ K}$, $\nu = 0.02\text{ T/s}$, and the lattice dimension is $10 \times 10 \times 10$.

m'	$B_{S,m'}^0\text{ (T)}$	$\Delta B_{S,m'}$	$P_{S,m'}^0$	$\langle P_{S,m'} \rangle$	$\sigma_{S,m'}^P$
-10	0.000000	6.5×10^{-15}	0.00000	0.00000	0.00000
-9	0.564160	1.6×10^{-6}	0	0.00000	0.00000
-8	1.099966	3.4×10^{-6}	0.00000	0.00000	0.00000
-7	1.612415	5.1×10^{-6}	0	0.00000	0.00000
-6	2.106511	6.7×10^{-6}	0.00138	0.00138	0.00001
-5	2.587260	7.9×10^{-6}	0	0.00002	0.00002
-4	3.059671	8.5×10^{-6}	0.01815	0.01835	0.00310
-3	3.528757	8.6×10^{-6}	0	0.22275	0.20795
-2	3.999529	7.8×10^{-6}	1.00000	1.00000	0.00000
-1	4.476997	6.3×10^{-6}	0	0.54270	0.33147
0	4.966165	3.9×10^{-6}	1.00000	1.00000	0.00015
1	5.472035	7.4×10^{-7}	0	0.99981	0.00929
2	5.999604	3.5×10^{-6}	1.00000	1.00000	0.00000
3	6.553867	8.6×10^{-6}	0	0.99990	0.00670

V. KEY ROLES OF DIPOLAR FIELDS

To investigate the effects of dipolar interactions, we divide the dipolar fields ($B_{ix}^{\text{di}}, B_{iy}^{\text{di}}, B_{iz}^{\text{di}}$) into two parts: transverse dipolar field (TDF) B_{ix}^{di} and B_{iy}^{di} , and longitudinal dipolar field (LDF) B_{iz}^{di} . TDF not only modifies $B_{m,m'}^i$, but also affects $\Delta_{m,m'}^i$ and $P_{m,m'}^i$. In contrast, LDF doesn't affect $\Delta_{m,m'}^i$ or $P_{m,m'}^i$, but shifts $B_{m,m'}^i$ by $-B_{iz}^{\text{di}}$. This means that LZ tunnelings actually occur at the field $B_{m,m'}^i - B_{iz}^{\text{di}}$, not $B_{m,m'}^i$. This shift has two effects. First, it broadens the LZ transition and thus make step risers deviate from the vertical direction in magnetization curves. Second, the quick changing of B_{iz}^{di} results in that the value $B_{m,m'}^i$ can be missed by the actual $B_z + B_{iz}^{\text{di}}$, and therefore the actual percentage of the reversed spins due to the LZ tunneling with respect to the total spins is smaller than the LZ probability $P_{m,m'}^i$ given in Eq. (8). This means that the dipolar interaction hinders both the direct LZ tunneling and the thermal assisted LZ tunneling.

Without TDF, $B_{m,m'}^i$ becomes $B_{m,m'}^0$, and $P_{S,m'}^i$ equals 0 for odd m' values because TDF is the only transverse term of odd order in Hamiltonian Eq. (4). Without LDF, the risers of steps become vertical and the percentage of the reversed spins due to LZ tunneling is strictly equivalent to the LZ probability $P_{S,m'}^i$ at low temperatures. These are shown by the dash-dotted line for 0.1 K

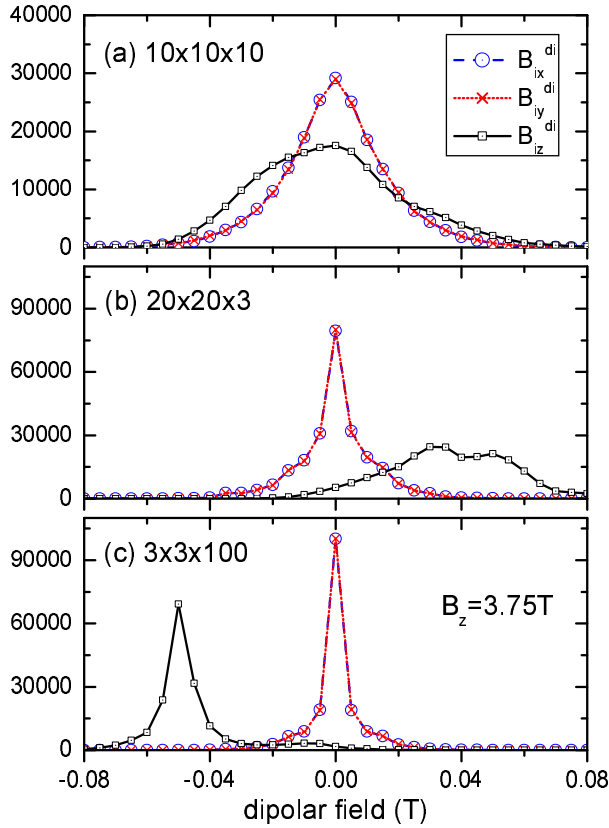


FIG. 5: (Color online.) Distributions of dipolar fields B_{ix}^{di} (dashed line + circle), B_{iy}^{di} (dotted line + cross), and B_{iz}^{di} (solid line + square) for the three lattice dimensions $10 \times 10 \times 10$ (a), $20 \times 20 \times 3$ (b), and $3 \times 3 \times 100$ (c) when the field B_z is swept to 3.75 T. The other parameters are $T = 0.5$ K and $\nu = 0.02$ T/s.

in Fig. 4. In Table I we also present the average value ($\Delta B_{S,m'} = \langle |B_{S,m'} - B_{S,m'}^0| \rangle$) of dipolar-field fluctuations with respect to $B_{S,m'}^0$, the dipolar-field-free LZ probability $P_{S,m'}^0$, and the average value $\langle P_{S,m'} \rangle$ and the corresponding standard error $\sigma_{S,m'}^P$ of $P_{S,m'}^i$ for the avoided crossing positions of S and m' , where m' varies from -10 to 3 and the averaging $\langle X \rangle$ of X^i is calculated over all the spins and all the runs. It should be pointed out that the $\Delta B_{S,m'}$ values, although very important, are very small, as shown in Table I. It is TDF that make $\Delta B_{S,m'}$ nonzero and make $P_{S,m'}^i$ ($m' = -5, -3, -1, 1, 3$) change from 0 to nonzero, even to nearly 1.

In order to elucidate the magnitude and distribution of the dipolar fields, we address the distributions of SMMs that have dipolar fields ($B_{ix}^{di}, B_{iy}^{di}, B_{iz}^{di}$), or in short the distributions of B_{ix}^{di}, B_{iy}^{di} , and B_{iz}^{di} , in the following. In Fig. 5 we compare the results from three different lattice dimensions $10 \times 10 \times 10$, $20 \times 20 \times 3$, and $3 \times 3 \times 100$. For the three lattices, our results show that the distribution of B_{ix}^{di} always is approximately equivalent to that of B_{iy}^{di} and they are both symmetrical and peaked at zero. The

peak becomes sharper when lattice dimension changes from $10 \times 10 \times 10$ to $20 \times 20 \times 3$ or $3 \times 3 \times 100$. The peak of the B_{iz}^{di} distribution is wider than that of both B_{ix}^{di} and B_{iy}^{di} . It can shift substantially away from zero when the lattice shape is very different from $L \times L \times L$, and can be seen from the positions of the step risers for the curves of different shapes at 0.1K in the inset of Fig. 4. The leftward shift of the B_{iz}^{di} peak can be attributed to dipolar-interaction-induced ferromagnetic orders in rod-like systems^{45,46}, and the similar rightward shift to anti-ferromagnetic orders in slab-like systems. Because dipolar interactions are the only inter-SMM interactions in our model, the differences of distributions between the the three lattices (box, slab and rod) are caused by the dipolar fields, or dipolar interactions in essence.

VI. CONCLUSION

In summary, we have combined the thermal effects with the LZ quantum tunneling effects in a DMC framework by using the giant spin approximation for spins of SMMs and considering magnetic dipolar interactions for comparison with experimental results. We consider ideal lattices of SMMs consistent with experimental ones and assume that there are no defects and axis-misalignments therein. We calculate spin reversal probabilities from thermal-activated barrier hurdling, direct LZ tunneling effect, and thermal-assisted LZ tunneling effects in the presence of sweeping magnetic fields. Taking the parameters of experimental Mn_{12} crystals, we do systematical DMC simulations with various temperatures and sweeping field rates. Our results show that the step structures can be clearly seen in the low-temperature magnetization curves, the thermally activated barrier hurdling becomes dominating at high temperature near 3K, and the thermal-assisted tunneling effects play important roles at the intermediate temperature. Our magnetization curves are satisfactory compared to experimental results, considering some possible defects and misalignments in the actual SMM samples.

Furthermore, our DMC results show that the magnetic dipolar interactions, with the thermal effects, have important effects on the LZ magnetization tunneling effects. Their longitudinal parts can partially break the resonance conditions of the LZ tunnelings and their transverse parts can modify the tunneling probabilities. They can clearly manifest themselves when the SMM crystal is extremely rod-like or slab-like. However, both the magnetic dipolar interactions and the LZ tunneling effects have little effects on the magnetization curves when the temperature is near 3K. This DMC approach can be applicable to other SMM systems, and could be used to study other properties of SMM systems.

Acknowledgments

This work is supported by Nature Science Foundation of China (Grant Nos. 10874232 and 10774180),

^{*} Corresponding author: bgliu@mail.iphy.ac.cn

¹ A. R. Rocha, V. M. García-suárez, S. W. Bailey, C. J. Lambert, J. Ferrer, and S. Sanvito, *Nature Mater.* **4**, 335 (2005).

² L. Bogani and W. Wernsdorfer, *Nature Mater.* **7**, 179 (2008).

³ M. N. Leuenberger and D. Loss, *Nature* **410**, 789 (2001).

⁴ M. Mannini, F. Pineider, P. Saintcavit, C. Danieli, E. Otero, C. Sciancalepore, A. M. Talarico, M.-A. Arrio, A. Cornia, D. Gatteschi, and R. Sessoli, *Nature Mater.* **8**, 194 (2009).

⁵ S. J. Koh, *Nanoscale Res. Lett.* **2**, 519 (2007).

⁶ T. Lis, *Acta Crystallogr., Sect. B* **36**, 2042 (1980).

⁷ R. Sessoli, D. Gatteschi, A. Caneschi, and M. A. Novak, *Nature* **365**, 141 (1993).

⁸ G. G. Condorelli, A. Motta, I. L. Fragalà, F. Giannazzo, V. Raineri, A. Caneschi, and D. Gatteschi, *Angew. Chem. Int. Ed.* **43**, 4081 (2004).

⁹ R. Zheng and B.-G. Liu, *J. Appl. Phys.* **106**, 054316 (2009).

¹⁰ G.-B. Liu and B.-G. Liu, *Appl. Phys. Lett.* **95**, 183110 (2009).

¹¹ L. Thomas, F. Lointi, R. Ballou, D. Gatteschi, R. Sessoli, and B. Barbara, *Nature* **383**, 145 (1996).

¹² J. R. Friedman, M. P. Sarachik, J. Tejada, and R. Ziolo, *Phys. Rev. Lett.* **76**, 3830 (1996).

¹³ J. R. Friedman, M. P. Sarachik, J. Tejada, J. Maciejewski, and R. Ziolo, *J. Appl. Phys.* **79**, 6031 (1996).

¹⁴ D. A. Garanin and E. M. Chudnovsky, *Phys. Rev. B* **56**, 11102 (1997).

¹⁵ I. Chiorescu, R. Giraud, A. G. M. Jansen, A. Caneschi, and B. Barbara, *Phys. Rev. Lett.* **85**, 4807 (2000).

¹⁶ W. Wernsdorfer, M. Murugesu, and G. Christou, *Phys. Rev. Lett.* **96**, 057208 (2006).

¹⁷ B. Barbara, L. Thomas, F. Lointi, I. Chiorescu, and A. Sulpice, *J. Magn. Magn. Mater.* **200**, 167 (1999).

¹⁸ W. Wernsdorfer, S. Bhaduri, A. Vinslava, and G. Christou, *Phys. Rev. B* **72**, 214429 (2005).

¹⁹ D. Gatteschi, R. Sessoli, and J. Villain, *Molecular nanomagnets*, Oxford University Press, New York 2006.

²⁰ A. L. Barra, D. Gatteschi, and R. Sessoli, *Phys. Rev. B* **56**, 8192 (1997).

²¹ A. Cornia, R. Sessoli, L. Sorace, D. Gatteschi, A. L. Barra, and C. Daiguebonne, *Phys. Rev. Lett.* **89**, 257201 (2002).

²² L. Landau, *Phys. Z. Sowjetunion* **2**, 46 (1932).

²³ C. Zener, *Proc. R. Soc. London, Ser. A* **137**, 696 (1932).

²⁴ H. De Raedt, S. Miyashita, K. Saito, D. Garcia-Pablos, and N. Garcia, *Phys. Rev. B* **56**, 11761 (1997).

²⁵ Q. Niu and M. G. Raizen, *Phys. Rev. Lett.* **80**, 3491 (1998).

²⁶ N. V. Vitanov and K.-A. Suominen, *Phys. Rev. A* **59**, 4580 (1999).

²⁷ W. Wernsdorfer, R. Sessoli, A. Caneschi, D. Gatteschi, and A. Cornia, *Europhys. Lett.* **50**, 552 (2000).

²⁸ V. L. Pokrovsky and N. A. Sinitzyn, *Phys. Rev. B* **65**, 153105 (2002).

²⁹ Z.-D. Chen, J.-Q. Liang, and S.-Q. Shen, *Phys. Rev. B* **66**, 092401 (2002).

³⁰ M. Jona-Lasinio, O. Morsch, M. Cristiani, N. Malossi, J. H. Muller, E. Courtade, M. Anderlini, and E. Arimondo, *Phys. Rev. Lett.* **91**, 230406 (2003).

³¹ Y.-C. Su and R. B. Tao, *Phys. Rev. B* **68**, 024431 (2003).

³² C. Wittig, *J. Phys. Chem. B* **109**, 8428 (2005).

³³ E. Rastelli and A. Tassi, *Phys. Rev. B* **64**, 064410 (2001).

³⁴ P. Földi, M. G. Benedict, J. M. Pereira, Jr., and F. M. Peeters, *Phys. Rev. B* **75**, 104430 (2007).

³⁵ H. C. Kang and W. H. Weinberg, *J. Chem. Phys.* **90**, 2824 (1989).

³⁶ K. A. Fichthorn and W. H. Weinberg, *J. Chem. Phys.* **95**, 1090 (1991).

³⁷ A. Cornia, A. C. Fabretti, R. Sessoli, L. Sorace, D. Gatteschi, A.-L. Barra, C. Daiguebonne, and T. Roisnel, *Acta Crystallogr., Sect. C* **58**, m371 (2002).

³⁸ Y. Li and B.-G. Liu, *Phys. Rev. Lett.* **96**, 217201 (2006).

³⁹ Y. Li and B.-G. Liu, *Phys. Rev. B* **73**, 174418 (2006).

⁴⁰ B.-G. Liu, K.-C. Zhang, and Y. Li, *Front. Phys. China* **2**, 424 (2007).

⁴¹ Eq. (7) can be obtained by solving equation $[1 - P(t)] \cdot R(t)dt = P(t + dt) - P(t)$, or $[1 - P(t)]R(t) = \frac{d}{dt}P(t)$, in the region $0 \leq t \leq \Delta t$, with initial condition $P(0) = 0$. For our case, $R(t)$ is independent of t in $[0, \Delta t]$.

⁴² R. D. Kirby, J. X. Shen, R. J. Hardy, and D. J. Sellmyer, *Phys. Rev. B* **49**, 10810 (1994).

⁴³ K. Saito, S. Miyashita, and H. De Raedt, *Phys. Rev. B* **60**, 14553 (1999).

⁴⁴ W. Wernsdorfer, C. R. Chim, *11*, 1086 (2008).

⁴⁵ D. A. Garanin and E. M. Chudnovsky, *Phys. Rev. B* **78**, 174425 (2008).

⁴⁶ D. A. Garanin, *Phys. Rev. B* **80**, 014406 (2009).